PERGAMON

Journal of Structural Geology 23 (2001) 1803–1819

JOURNAL OF STRUCTURAL GEOLOGY

www.elsevier.com/locate/jstrugeo

The geometric and statistical evolution of normal fault systems: an experimental study of the effects of mechanical layer thickness on scaling laws

Rolf V. Ackermann[a,b,*], Roy W. Schlische[c], Martha O. Withjack[a,c]

[a]*Formerly at: Mobil Technology Company, P.O. Box 650232, Dallas, TX 75265-0232, USA*
[b]*ExxonMobil Upstream Research Company, P.O. Box 2189, Houston, TX 77252-2189, USA*
[c]*Department of Geological Sciences, Rutgers University, Piscataway, NJ 08854-8066, USA*

Received 16 September 1999; revised 18 January 2001; accepted 15 February 2001

Abstract

Detailed analyses of two scaled experimental models of distributed extension that differ only in the thickness of the mechanical layer reveal how normal-fault systems evolve with increasing strain. Faults grow increasingly by linkage and become regularly spaced; the proportion of active structures decreases and converges with that of inactive structures. Large faults contribute increasingly to strain accommodation. The size-frequency distribution of fault lengths changes from power-law (fractal) to exponential, non-linear and dynamic length-displacement scaling arises, and the system becomes less multifractal and more homogeneous. These observations validate many predictions of numerical and geometric models of normal fault growth and system evolution. We propose a generalized three-stage model in which mechanical stratigraphy at times restricts fault growth and the degree of elastic fault interaction. The *thickness* of the mechanical layer influences the relative timing of stages in this model, as well as the geometry and statistics of the system. As faults encounter and breach multiple mechanical layers, systems may exhibit different scaling attributes at different structural or mechanical levels. Thus, systems may oscillate between different stages of this model, complicating fault-population statistics. We present our data as evidence of the existence of upper and lower bounds for the scale invariant behavior of fault systems, as predicted by Mandelbrot for natural fracture systems.

Keywords: Mechanical layer; Scaling law; Fault systems; Experimental modelling

1. Introduction

Fault-population systematics integrates statistical description of fault attributes (e.g. fault displacement, trace length) and spatial-analysis techniques to gain a better understanding of the whole fault population. The work of Marrett and Allmendinger (1991, 1992), Walsh et al. (1991) and Gauthier and Lake (1993) marked the beginning of the practical application of fault-population systematics. They provided fractal-based methods for estimating the number of faults not imaged by seismic data. More recently, Pickering et al. (1997) estimated the dimensions of unimaged fault tips in the southern North Sea, calibrated with outcrop data. Other applications have included generating a structural history by breaking out subsets of structures based on their statistical distributions (Ackermann and Schlische, 1997), and providing input and constraints for models of fault growth and interaction (Cowie and Scholz, 1992a,b; Gupta and Scholz, 1998). Many studies have focused on how fault-population data are affected by fault type (Wojtal, 1994), geologic setting (Cowie et al., 1995; Gross et al., 1997a), fault linkage (Trudgill and Cartwright, 1994; Cartwright et al., 1995; Dawers and Anders, 1995; Wojtal, 1996), and mechanical stratigraphy (Gross, 1995; Gross et al., 1997b; Ackermann et al., 2001).

The aforementioned studies deal with scaling laws derived from fault-population data. Comparisons of multiple data sets commonly result in what many accept as general scaling laws (e.g. relations between fault length and displacement; Cowie and Scholz, 1992a,b; Dawers et al., 1993; Schlische et al., 1996; Ackermann and Schlische, 1999). It is not clear, however, if many of these laws are universal. If the laws are related to processes, and the processes change with time and strain, then the laws may

* Corresponding author. Correspondence address: ExxonMobil Upstream Research Company, P.O. Box 2189, Houston, TX 77252-2189, USA. Tel.: +1-713-431-7073.

E-mail addresses: rolf_v_ackermann@email.mobil.com (R.V. Ackermann), rvacker@upstream.xomcorp.com (R.V. Ackermann).

0191-8141/01/$ - see front matter
PII: S0191-8141(01)00028-1

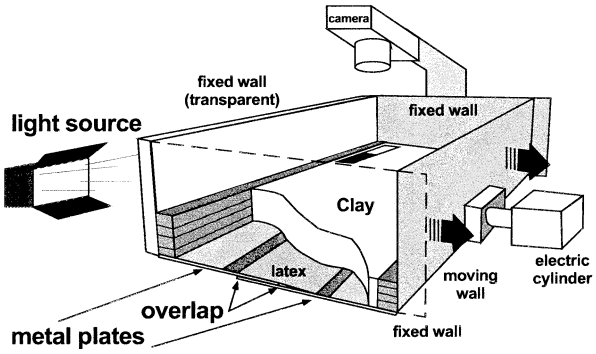

Fig. 1. Modeling apparatus. Modified from Eisenstadt and Withjack (1995).

change accordingly. It is also not yet clear whether scaling laws hold at all scales (Jackson and White, 1989; Scholz and Contreras, 1998; Ackermann and Schlische, 1999; Marrett et al., 1999).

To address these issues, researchers have used geometric (e.g. Cladouhos and Marrett, 1996), numerical (e.g. Cowie et al., 1993; 1995; Cowie, 1998), and experimental models (e.g. Kautz, 1987; Kautz and Sclater, 1988; Davy et al., 1995; Fossen and Gabrielsen, 1996; Ackermann, 1997; Marchal et al., 1998; Spyropoulos et al., 1999; Clifton et al., 2000) to simulate the development of structural systems. In this study, we pursue an experimental approach. Specifically, we use geometric, statistical, and fractal methods to fully characterize the development of an experimental population of normal faults through time. Our work provides an independent validation of published geometric and numerical studies of fault-population development. Also, it complements previous experimental studies which examined normal-fault populations in cross-sectional view (e.g. Kautz and Sclater, 1988; Fossen and Gabrielsen, 1996), at a single stage of development (e.g. Clifton et al., 2000), or with different modeling media (e.g. Fossen and Gabrielsen, 1996; Marchal et al., 1998). Our experimental design is similar to that of Spyropoulos et al. (1999), who also studied fracture development with increasing strain. Our experiments differ from those of Spyropoulos et al. (1999) in that ours are scaled and calibrated to maintain dynamic similarity with nature. Also, our experiments produced shear fractures (faults), whereas the experiments of Spyropoulos et al. (1999) produced opening-mode fractures.

2. Experimental and analytical approach

2.1. Experimental design and scaling

For more than 70 years, geologists have used experimental models with wet clay, dry sand, and wet plaster to simulate normal faulting (e.g. Cloos, 1928, 1930, 1968; Oertel, 1965; Withjack and Jamison, 1986; Vendeville, 1987; Kautz and Sclater, 1988; Ellis and McClay, 1988; Withjack et al., 1995). We selected wet clay as the modeling material in our experiments. The wet clay has a coefficient of internal friction of about 0.5 and a cohesion of about 50 Pa (Sims, 1993; unpublished work by Furgo-McClelland, Inc., 1992, and by S. Dixon, 1996). Its density is approximately 1.6 g cm^{-3}, it is approximately 40% water by weight, and it is composed predominantly of kaolinite. Wet clay deforms by both distributed cataclasis and discontinuous cataclastic faulting. Faults are numerous, and fault zones are narrow and well defined.

The modeling apparatus has a horizontal metal base, three vertical fixed walls, and one vertical moveable wall (Fig. 1). Two, overlapping, metal plates cover the metal base. The top plate is attached to the moveable wall, whereas the bottom plate is attached to the opposing fixed wall. A thin, rubber sheet, 12.5 cm wide, straddles the metal plates. One edge of the rubber sheet is attached to the top plate, whereas the other edge is attached to the bottom plate. A layer of wet clay covers the metal plates and rubber sheet. The thickness of the clay layer is 1.8 cm in the 'thin' model and 3.6 cm in the 'thick' model. During the models, we displace the moveable wall and the attached metal plate at a constant rate of 5 cm hr^{-1}. In response, the overlying rubber sheet and the clay layer stretch at a strain rate of 0.4 hr^{-1}.

To ensure dynamic similarity between the models and natural prototypes, two conditions must be satisfied. First, the modeling material and the rocks in nature must have similar coefficients of internal friction (e.g. Nalpas and Brun, 1993; Weijemars et al., 1993). This condition is satisfied with wet clay as the modeling material. Second,

$$C^* = \rho^* \times g^* \times l^* \quad (1)$$

where C^*, ρ^*, g^*, and l^* are model-to-natural prototype ratios for cohesion, density, gravity, and length, respectively (e.g. Hubbert, 1937; Weijemars et al., 1993; Vendeville et al., 1995). In our models, the values of ρ^* and g^* were about 0.7 and 1.0, respectively. C^* was about 10^{-4} to 10^{-5}. Thus, to ensure dynamic similarity between the models and nature, l^* was 10^{-4} to 10^{-5} (i.e. 1 cm in the models equaled 100–1000 m in nature).

Although the criteria for dynamic similarity are satisfied, we emphasize that the experimental models are not exact scale models. Rock may deform differently than the clay in the models. For example, rock with pre-existing heterogeneities (e.g. faults, fractures, bedding) may behave very differently than the homogeneous clay in the models. A wealth of previous experimental studies, however, show that properly designed experiments realistically simulate many extensional tectonic processes (e.g. Cloos, 1968; Withjack and Jamison, 1986; Vendeville, 1987; Withjack and Callaway, 2000).

2.2. Analytical approach

Our analytical approach involves using geometric, statistical, and fractal methods to characterize the fault systems in

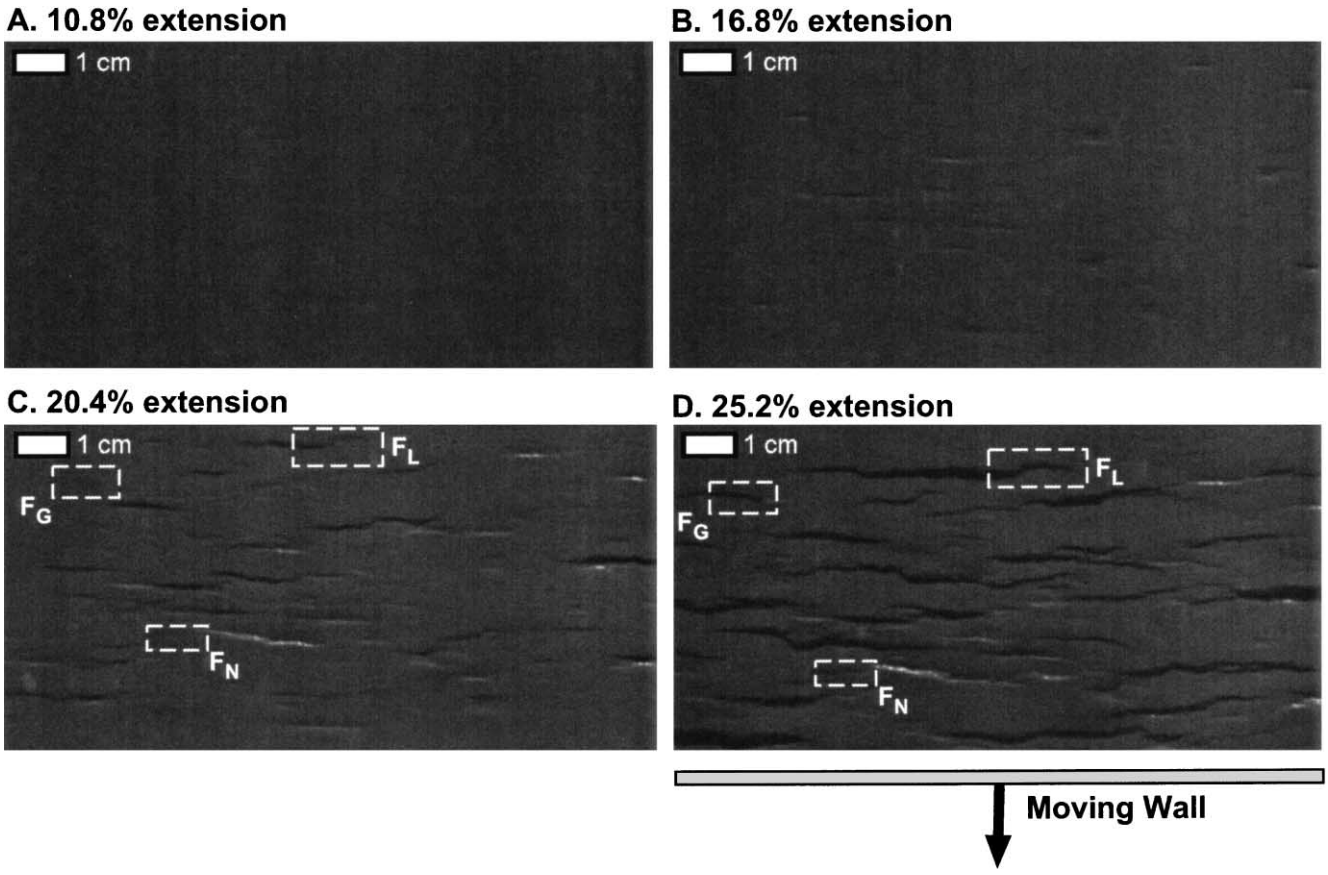

Fig. 2. Detail of the thick model, showing the evolution of the fault pattern. See Fig. 3 for location within entire model. Light source is located at the top of the figure; thus, faults dipping toward the top of the figure appear white, whereas those dipping toward the bottom of the figure are dark. Examples of the different subdivisions of fault type are shown in (C) and (D): new faults (F_N), faults that grew (F_G), and faults that linked (F_L).

the models of simple distributed extension. To record the deformation patterns in the clay layer through time, we photographed its top surface at regular increments (0.15 cm of displacement of the moveable wall). The top surface was displaced by shear fractures (faults) that have tool-and-groove slickenlines, and dip about 60°. We later scanned the central region of the photographic images at 4000 dpi (dots per inch), cropping out edge effects associated with the apparatus walls and the edges of the rubber sheet (see Fig. 6). Thus, each image is akin to a finite study area within a larger area. Using Scion IMAGE software, we calculated the tip-to-tip trace length, fault displacement, and the centroid coordinates of all the normal faults at each displacement increment. We analyzed the data generated from the sequential fault trace maps relative to the extension imposed on the model, thus showing the evolution of the fault system.

3. Results

3.1. Map patterns and fault activity

In both the thick and thin layer models, the fault pattern steadily developed as strain increased (Figs. 2 and 3). New normal faults continually emerged, some becoming inactive as extension increased. Other faults remained active for a prolonged time, growing in terms of displacement and length, and linking with other normal faults (Fig. 2). The total number of visible faults initially increased as extension increased in both models (Fig. 4A), and began to level off at about 18 and 21% extension in the thin and thick models, respectively. This experimental result resembles that predicted numerically by Cowie et al. (1995) and geometrically by Cladouhos and Marrett (1996).

To better understand fault-pattern development in the models, we subdivided the fault population (F_T, total number of faults) into several categories: new faults (F_N), faults that grew by propagation (F_G), faults that linked (F_L), active faults (F_A), and inactive faults (F_I). This analysis showed that fault linkage was not measurable at the free surface until about 15 and 17% extension in the thin and thick model, respectively (Fig. 4B). The rate of fault linkage increased in both the thin and thick model at about 18 and 20% extension, respectively. The relative number of new faults generally decreased with increasing extension (Fig. 4C). In both models, the relative abundance of inactive faults increased with increasing extension (Fig. 4D). The

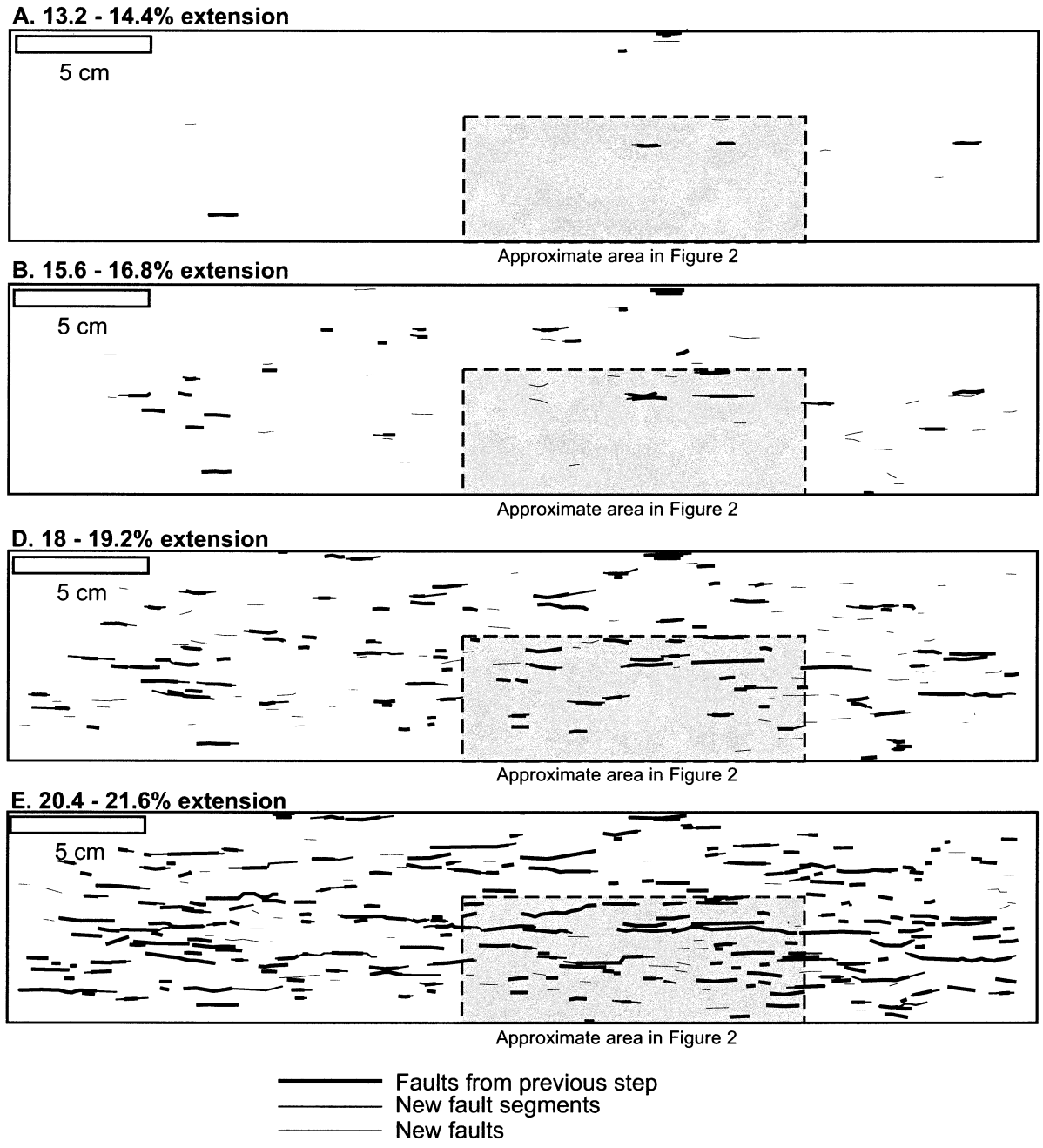

Fig. 3. Fault trace maps (footwall cutoffs) for the thick model. Structures are shaded/coded by type and age. Areas shown in details in Fig. 2 are outlined.

relative abundance of active and inactive faults was approximately the same in both models for a given amount of extension.

3.2. Fault length data

In both the thin and thick models, the average (arithmetic mean) observed fault length (L_{avg}) increased steadily with increasing extension (Fig. 5A). The maximum observed fault length (L_{max}) also increased steadily, but with a significant jump at ~13% extension in the thin model and ~16% in the thick model (Fig. 5B). L_{max} then levels off at ~17% extension in the thin model, but only dips temporarily in the thick. Interestingly, this trend is similar to that of correlation length when the percolation threshold (for the bond percolation problem) is approached (see Stauffer and Aharony, 1992), e.g. the biggest fault (including soft-linkage) begins to cross the entire region (in this example, the model). The sum of the lengths of all the faults in the model (ΣL) is a convenient proxy for the degree of discontinuous deformation (rupture area) in the models. ΣL increases in a similar manner in both models, increasing rapidly at ~14% extension in the thin model and at ~16% in the thick model (Fig. 5C). This is the same pattern observed in the

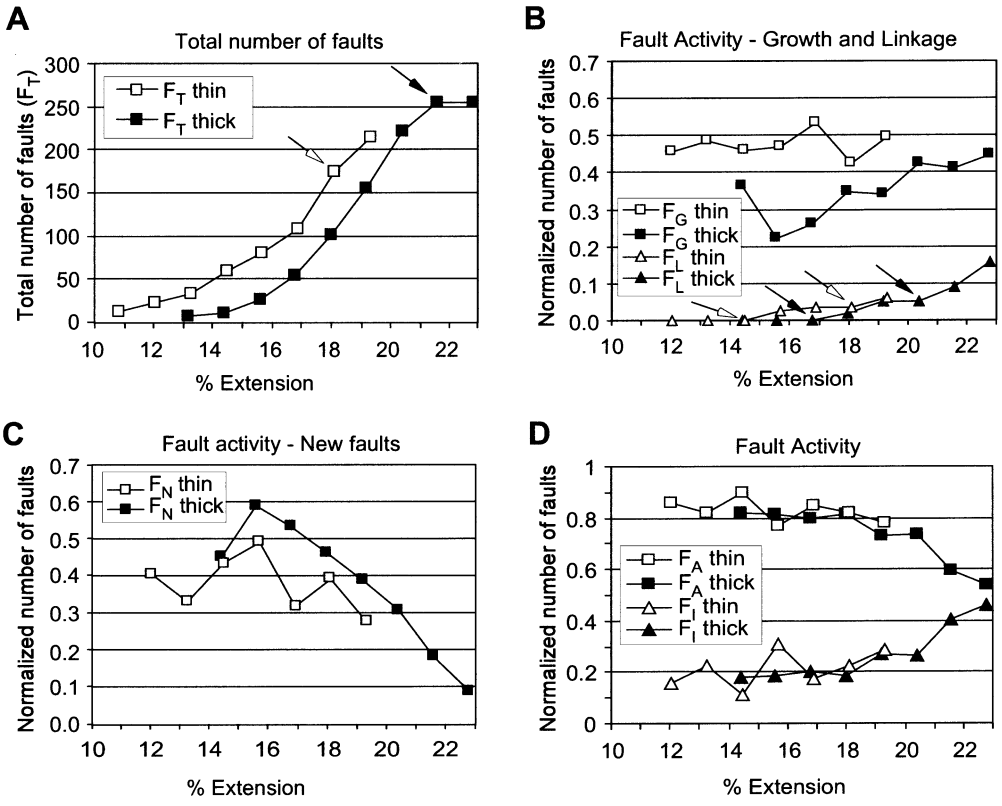

Fig. 4. Fault activity data. (A) Total number of faults (F_T) observed during model runs. (B) Fault activity in terms of number of faults that grew by propagation (F_G) or linkage (F_L). (C) Fault activity in terms of number of new faults (F_N). (D) Fault activity in terms of active (F_A) and inactive (F_I) faults. An active fault is one that grew by propagation (F_G), linkage (F_L) or was new (F_N); all others are inactive. Values in (B), (C) and (D) are normalized to the total number of faults (F_T) for a given extension increment (otherwise all values increase continually). Note how the values of F_A and F_I converge. Arrows point to inflections discussed in text.

geometric models of Cladouhos and Marrett (1996). At a given extension, the values of L_{avg}, L_{max}, and ΣL are always greater in the thin model than in the thick (Fig. 5). Thus, the thin model has more faults and those faults are longer than those in the thick model at the same strain.

3.3. Cumulative frequency of fault lengths

Studies of faults and their scaling relationships use displacement or trace length data. In this study, we refer to fault scarp height (throw) as displacement, because our faults exhibit tool-and-groove slickenlines that rake 90°. We refer to the footwall cutoff trace length exposed on the model surface as the trace length. Four types of size-frequency distributions are commonly reported for fracture data (e.g. Rives et al., 1992). Normal and log-normal are usually reported for joints and veins, whereas power-law and exponential have been reported for faults, joints, and veins.

Fracture size-frequency data are usually displayed in log–log or log–linear space in order to identify sampling artifacts that stem from exposure, sampling area dimensions, and sampling resolution. All fault length data, regardless of data acquisition method, suffer from sampling artifacts. For example, unless a fault nucleates at the structural level of observation, it is not possible to sample its maximum trace length (Fig. 6A). This is exacerbated when multiple faults are hard-linked, as in the breaching of a relay ramp (Fig. 6B), and the faults have not nucleated at the same level. Fig. 6B defines trace length for hard-linked normal faults in this study.

Other sampling artifacts stem from sampling area dimensions (data censoring) and imaging resolution (data truncation), and are best described in the context of cumulative frequency analysis (Fig. 6). The faults on the map in Fig. 6A are shaded according to how they are sampled. First, there are small faults whose maximum displacement is below the resolution of data acquisition method (e.g. 30 m throw on a moderately dipping fault imaged in the North Sea with high-frequency seismic). This is data truncation (Pickering et al., 1995). This imaging limitation affects the tips of faults as well, where, depending on the displacement gradient (e.g. Cowie and Shipton, 1998), a certain length of the fault will not be imaged, thus underestimating the fault-trace length and/or height (Fig. 6A); this is type C censoring. Finally, some faults are so long that they extend beyond the study area boundaries, causing their lengths to be undersampled; this is type B censoring (Pickering et al., 1995). The statistical expression of these artifacts is shown in Fig. 6B. The type of

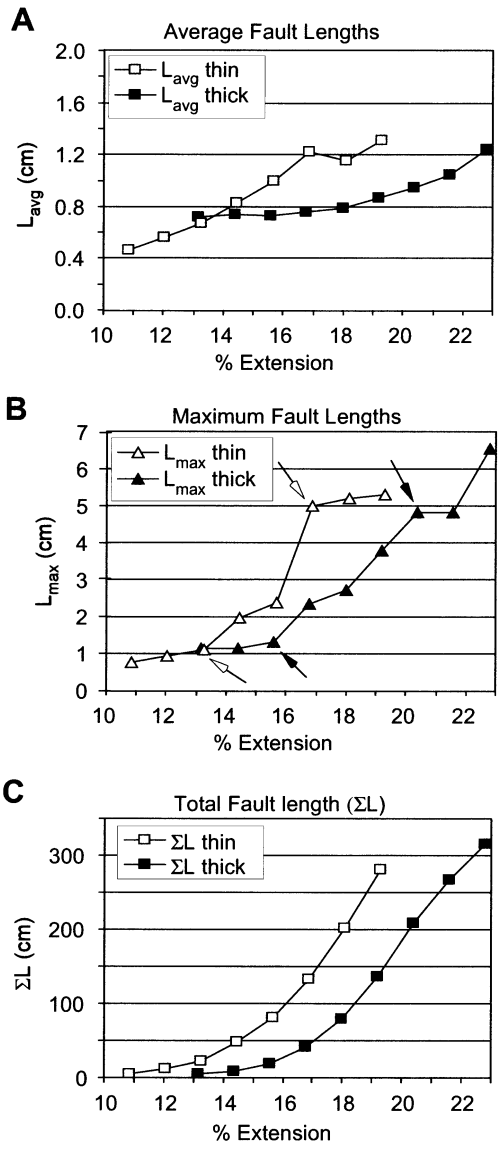

Fig. 5. Fault length data. Average (L_{avg}) (A) and maximum (L_{max}) (B) fault length data for model runs. (C) Total fault length (ΣL) for model runs. Arrows point to inflections discussed in text. Note that early inflections in L_{max} are roughly coeval with the onset of linkage (F_L, Fig. 4).

distribution applied is based on goodness-of-fit and curve shape: a power-law distribution, excluding sampling artifacts, plots as a straight line in log–log space, whereas an exponential distribution plots as a curved line in log–log space. The data used to generate the curves are bounded at high values by the truncation artifact, and at low values by the two censoring artifacts.

Some continental fault populations obey a power-law (fractal) distribution of size such that:

$$N(L) \geq aL^{-\varphi_f} \quad (2)$$

where $N(L)$ is the total number of faults with dimensions greater than or equal to L (e.g. Kakimi, 1980; Marrett and Allmendinger, 1992; Scholz et al., 1993; Wojtal, 1994; Pickering et al., 1995). φ_f may be referred to as the power-law exponent, fractional (fractal) dimension, or fragmentation dimension. Steeper slopes (thus greater values of φ_f) indicate that smaller structures are relatively more important than larger structures in strain accommodation (Scholz and Cowie, 1990; Pickering et al., 1995). Wojtal (1996) and Ackermann and Schlische (1997) have argued that size-frequency distributions of some natural fault populations possess two distinct central segments, which correspond to two distinct size-frequency distributions, as a result of fault linkage or the presence of sub-populations. Values for φ_f depend on sampling scheme and whether faults are constrained or unconstrained (Marrett and Allmendinger, 1991; Ackermann and Schlische, 1997).

Cowie et al. (1994) showed that the size distribution of normal faults in oceanic crusts is best described by an exponential function, although in the zone of active faulting immediately adjacent to the ridge (±10 km) a power-law distribution is more appropriate (Cowie et al., 1994), i.e.

$$N(L) \geq N_T e^{-\lambda L} \quad (3)$$

where $N(L)$ is again the number of faults with length greater than or equal to L, N_T is the total number of measurements, and λ is inverse of $\langle L \rangle$, the characteristic (or mean) value of L. λ is also the slope of the best-fit line for the data. The definition of a mean value or characteristic size is a diagnostic feature of exponential distributions (Cowie et al., 1994).

Fig. 7 shows the fault-length cumulative-frequency data at different time steps for the two models. For both models, data at lower strains are best fit using a power-law relationship, whereas at higher strains an exponential relationship provides a better fit. Spyropoulos et al. (1999) also found this transition in their experimental models of opening-mode fractures, and Gupta and Scholz (2000) observed this transition in the Afar depression. The type of size distribution is unclear at moderate strains; during this transition there may be more than one size-frequency distribution present. The transition from power-law to exponential occurs at a lower strain in the thin model (~14–15% extension) than in the thick model (~19%). ⟨L⟩ is compared with L_{avg} in the insets of Fig. 7. Note that ⟨L⟩ is consistently less than L_{avg}, consistent with the sampling issues raised above. This relationship suggests that there are very small faults below the model surface (e.g. Viersma, 1997).

It is interesting to note that the value of φ_f in the power-law relationship generally decreases with increasing strain in both models (Fig. 7), pointing to an increase in the importance of large faults in strain accommodation. This trend is consistent with those in the experimental models of Sornette et al. (1993). It also matches those predicted numerically by Sornette and Davy (1991) and Cowie et al. (1995), and geometrically by Cladouhos and Marrett (1996).

3.4. Length-displacement scaling

The relation between maximum observed displacement,

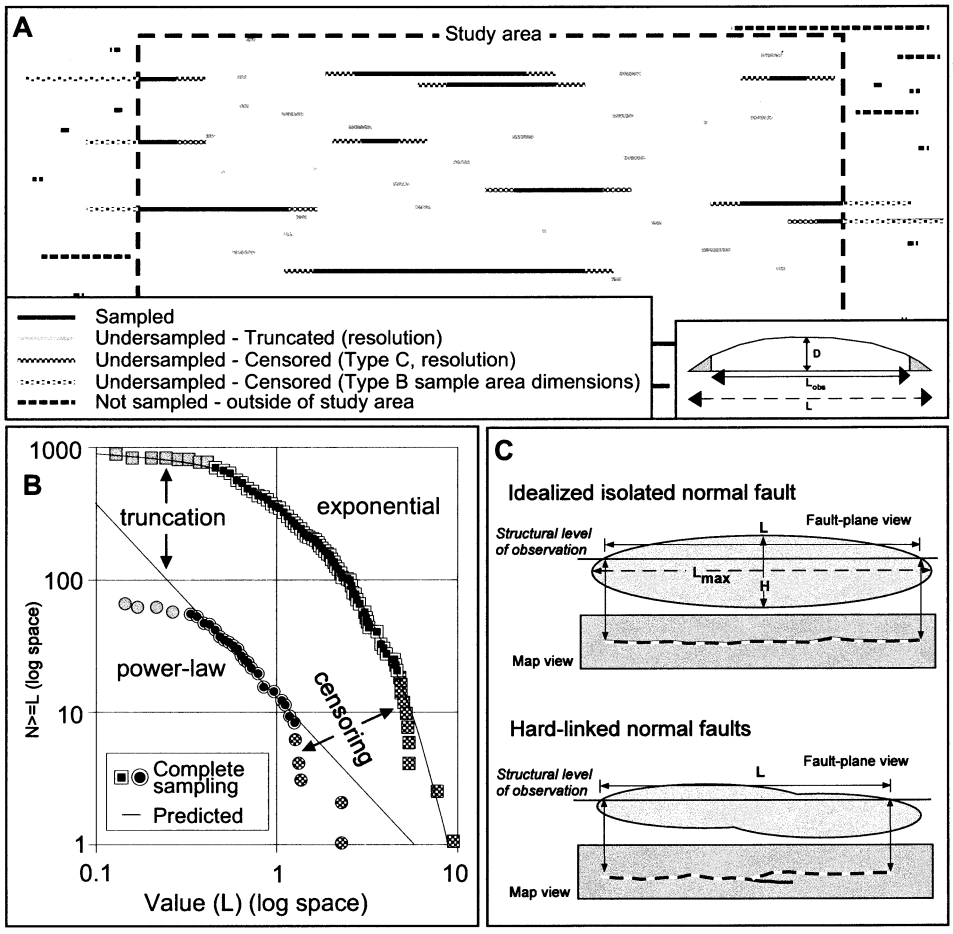

Fig. 6. Sampling artifacts and cumulative frequency analysis. (A) Map-view definitions of sampling and truncation, and their effects on the sampling of systems (map) and individual faults (inset). (B) Examples of the two fault size distributions described in this report, based on cumulative frequency ($N(L) \geq L$). The data in (B) are shaded using the key in (A). The data used to generate the curves are bounded at high frequency by a truncation artifact and at low frequency by censoring artifacts. (C) Definition of fault length and sampling problems. For an idealized normal fault, observed length (L) is less than true length (L_{max}) because structural level of observation is not the same as the nucleation level. Hard linked normal faults suffer from the same problem as isolated ones, exacerbated by differing nucleation levels. Map-view trace lengths are shown with a dashed line at the bottom of both parts of (C).

D, and trace length, L, has been the topic of much discussion in the geologic literature in the last 10 years. This relation,

$$D = \gamma L^n \tag{4}$$

where γ is related to rock properties (dominantly shear strength of the rock and elastic rigidity, see Gillespie et al. (1992), Cowie and Scholz (1992b) and Cowie (1998)), and n is an exponent. Early work found $n > 1$ (Watterson, 1986; Walsh and Watterson, 1988; Gillespie et al., 1992; Marrett and Allmendinger, 1992), but later studies have converged on $n = 1$ (Cowie and Scholz, 1992b; Dawers et al., 1993; Villemin et al. 1995; Schlische et al., 1996). The only work thus far to have found $n < 1$ was Fossen and Hesthammer (1997) for shear bands, Gross et al. (1997b) for faults influenced by mechanical stratigraphy and accommodating strain via block rotation, and Davy et al. (1995) for reverse faults produced in uniaxial shortening analog experiments. A value of $n < 1$ suggests that large faults lengthen more quickly per unit displacement than small faults.

Our experimental data indicate that $n < 1$ (Fig. 8). Both n and γ generally decrease with increasing extension. This indicates that with increasing strain in the models, faults lengthen more rapidly per unit displacement, consistent with the notion of fault linkage. Values of n and γ are lower for the thin model than the thick, at a given strain. Thus, the faults in the thin model lengthen more rapidly per unit displacement, and have higher aspect ratios than those in the thick model. This is consistent with the L_{avg}, $L_{max,}$ and ΣL data presented in Fig. 5.

3.5. Fault spacings

Fault spacings are usually measured along scanlines oriented perpendicular to the dominant fault strike. The average spacing was calculated for each scanline, then all scanlines were averaged to obtain s_{avg}, the average fault spacing for the study area. This assumes minimal lateral variations in strain accommodation. Early in the model runs, the data are variable and noisy as the model begins to fill in with structures, but then spacings decrease steadily

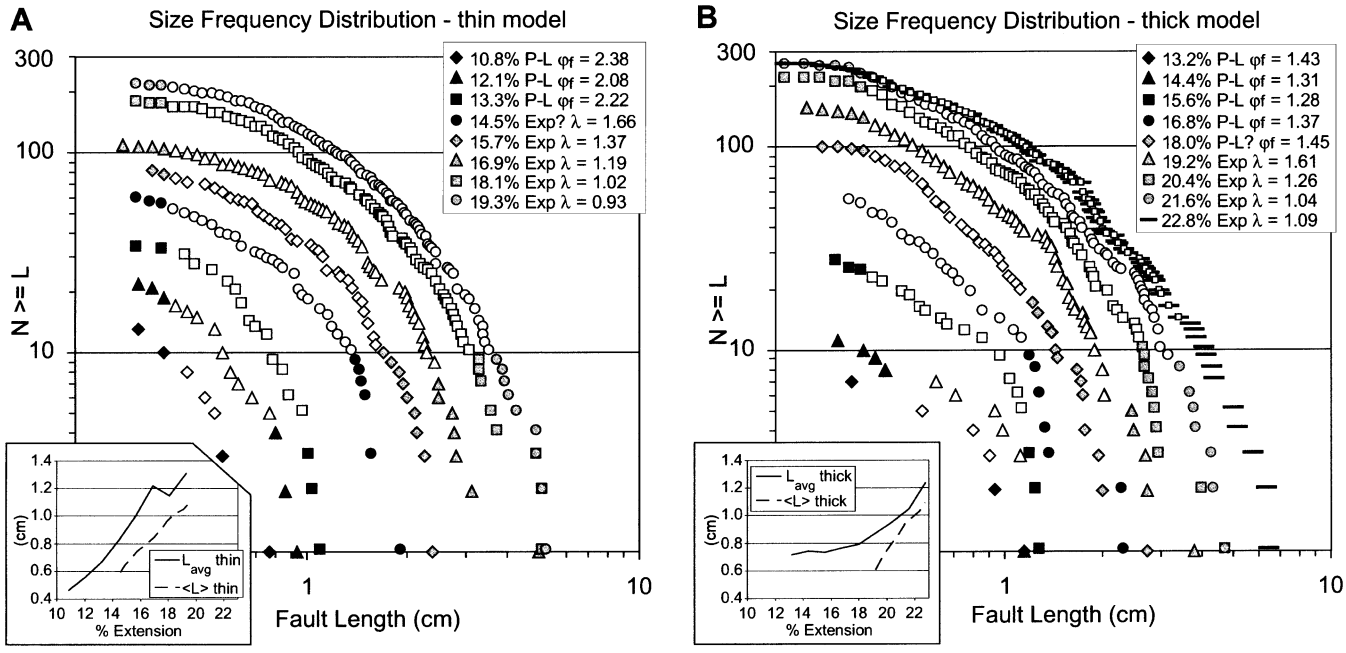

Fig. 7. Cumulative fault length-frequency distributions for the thin model (A) and the thick model (B). Data used for generating curve fits are represented by open symbols. Notice that all time steps suffer from data truncation and censoring (see Fig. 5). Distribution types and exponent values are shown in upper inset. ⟨L⟩ derived from λ is compared with L_{avg} in lower insets.

with increasing extension, appearing to level off toward the end of the model run (Fig. 9A). The average standard deviation of fault spacings (r) provides a measure of their regularity: a smaller standard deviation indicates that faults are more regularly spaced. With increasing extension, fault spacings become steadily more regular, also appearing to level off toward the end of the model run (Fig. 9B). Thus, as the system evolves, fault spacing generally decreases and becomes more regular, analogous to the behavior of opening-mode fractures as the system matures and approaches saturation (e.g. Wu and Pollard, 1995).

3.6. Spatial distribution of fault centroids

The spatial distribution of faults and fault centroids (a centroid is the center of the fault ellipse, projected up-dip or down-dip to the structural level of observation) through time was assessed using a nearest-neighbor method from Cressie (1993) and Swan and Sandilands (1995). This method compares the mean observed nearest neighbor distance (O_d) between centroids with an expected (O_δ) (Fig. 10) based on a Poisson (random) distribution:

$$O_d/O_\delta = \Omega \tag{5}$$

where Ω is the nearest-neighbor statistic. Values of Ω range from 0 (clustered point pattern) to 2.15 (regular point pattern), with values of 1 indicating randomness and 2 indicating uniformity. Ω can fall between these values (Fig. 10), thus revealing tendencies or overprints, e.g. a random point distribution with a tendency toward uniformity.

Fig. 11 summarizes the results of the analysis and the implications of the value of Ω. The data are noisy early in the model run, either because of edge-effects in the spatial statistics as summarized in Swan and Sandilands (1995), or because there is no clear trend. The data become more coherent midway through the model runs, with values of Ω indicating an essentially random distribution of centroids.

The nearest neighbor analysis was also performed on centroid maps of active structures and inactive structures. Comparing these Ω values with those for only active or inactive structures gives a measure of the degree to which each subpopulation is affecting the distribution of centroids, e.g.

$$\Omega_{AR} = \Omega - \Omega_A \tag{6}$$

where Ω_{AR} is the active faults nearest neighbor residual and Ω_A is the nearest neighbor statistic for active centroids.

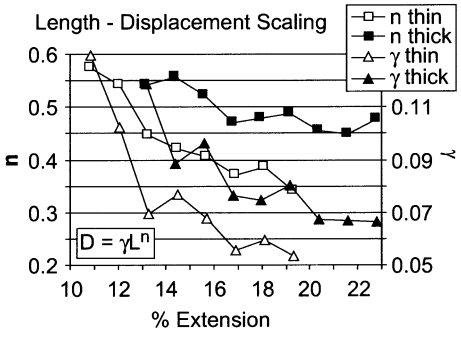

Fig. 8. Length-displacement scaling data for both model runs. Notice how scaling changes with increasing strain, and was not observed to be linear ($n \neq 1$).

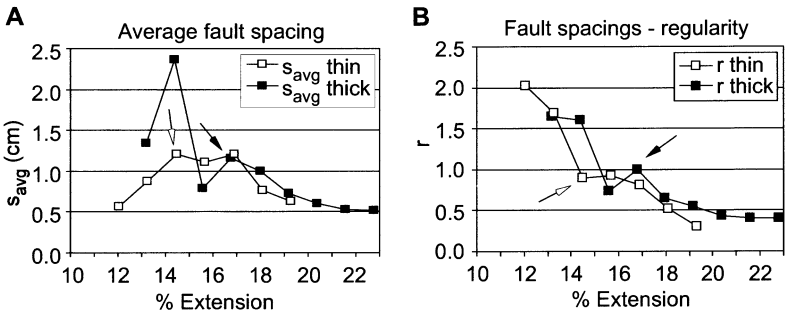

Fig. 9. (A) Average fault spacing (s_{avg}) for both model runs. (B) Average fault spacing standard deviation data (r) for both model runs. Lower values of r indicate more regular spacing. Arrows point to inflections discussed in text.

Thus $\Omega_{AR} = 0$ suggests that the active subpopulation is dominant (Fig. 12A). Interestingly, $\Omega_{AR} = 0$ for the same extension ranges in both models. The departure of Ω_{AR} from ~0 is coeval with increased proportions of inactive faults.

3.7. Fractal analysis of fault trace maps

Although Ω and Ω_{AR} provide information about the distribution of centroids and how they interact, they do not reveal very much about how the fault traces themselves are distributed. Box-counting methods that assess the map pattern, however, do provide such information. The changing map pattern of the model can be viewed as a series of realizations in two-dimensional space. To paraphrase Gauthier and Lake (1993): if the geometry, frequency, and distribution of the elements of an object (e.g. a fault map) are scale invariant, that object can be classified as a fractal (*sensu* Mandlebrot, 1967). Scale invariance means that the object looks fundamentally the same at all scales of observation, e.g. seismic, aerial photography, outcrop. For map patterns, we examine the size-frequency distribution of boxes containing faults for grids of varying size. For our purposes, we do not examine fractal geometry (e.g. the ruler dimension of coastlines).

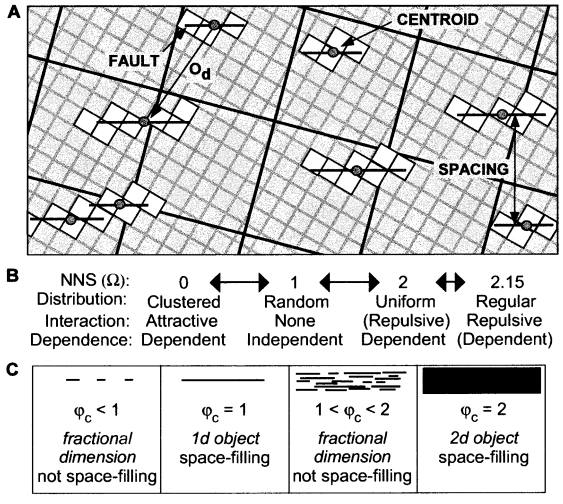

Fig. 10. Methods of spatial characterization used for analyzing fault patterns in the models. (A) Fault map showing faults and centroids. Definition of fault spacing is shown in lower right. For the nearest neighbor analysis, observed nearest neighbors are shown. For the fractal analyses, two grids of different sizes are shown, oriented so as to minimize the number of cells needed to cover the map; cells that count as occupied are highlighted in white. (B) Range of nearest neighbor statistic (Ω) values, and their implications for point interaction and dependence. For example, a random distribution implies independence of points, and hence no interaction (Cressie, 1993; Swan and Sandilands, 1995). Thus, the geologic process determining the positions of centroids is blind to the positions of other centroids. For non-random distributions, the establishment of a point (centroid) changes the probability of another one occurring in the vicinity. (C) Examples of sets that have fractional (fractal) dimensions. A fractal dimension that has an integer value is equivalent to a Euclidean dimension.

Two fractal box-counting methods for analysis of (potentially) self-similar patterns were used. The capacity dimension is defined as the exponent φ_c in the relationship:

$$N(\nu) = (\nu^{\varphi_c})^{-1} \tag{7}$$

where $N(\nu)$ is the number of boxes of linear size ν necessary to cover a data set of points distributed in a two-dimensional plane. For Euclidean objects, this equation yields their dimension, φ (which, if not an integer, yields a *fractional* dimension; hence the term *fractal dimension*). A grid oriented to minimize the number boxes needed to cover the map (Fig. 10) is placed over it, and the number of boxes occupied by faults are counted for a range of box sizes (ν). If the set is fractal, the data will follow a power-law size-frequency distribution, with a slope that equals $-\varphi_c$. The information dimension, (φ_i) is calculated in the same manner, except that each box is weighted by the amount of fault-trace length that falls within it. By definition, $\varphi_c < \varphi_i$. Greater values of φ_c and φ_i indicate that the object is more space-filling (Fig. 10).

All of the box-counting analyses indicate that the maps are fractal. The results of the capacity dimension (φ_c) box counts are provided in Fig. 12B, which shows that the fractal dimensions for the two systems increase systematically, with a change in the trend at 15 and 18% extension in the thin model, and at 16 and 20% extension in the thick model. φ_c is always greater for the thin model, implying that the map is filled with more fault length, consistent with the ΣL data (Figs. 5 and 12). These data are consistent with the

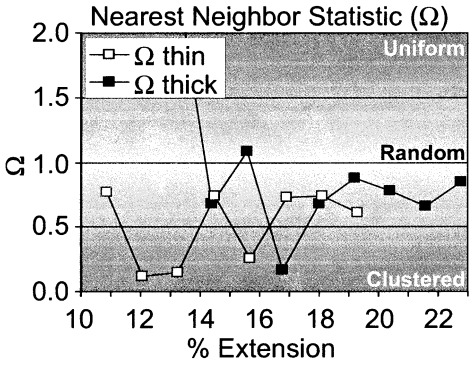

Fig. 11. Nearest neighbor statistic values for centroid maps from both model runs. Values of 0, 1, and 2 for Ω indicate clustering, randomness, and uniformity in the point distribution, respectively. Implications for point interaction (dependent, repulsive, etc.) are noted.

numerical predictions of Cowie et al. (1995). The information dimension (φ_i) follows the same trend as φ_c (Fig. 12C), and φ_i is always greater than φ_c.

3.8. Multifractals

Following Cowie et al. (1995), a system is a multifractal when a fractal (power-law) size distribution is superimposed on a fractal map pattern. Departure from $\varphi_c = \varphi_i$ is indicative of this. We can derive a multifractal index (I_m):

$$I_m = \varphi_i - \varphi_c \quad (8)$$

Lower values of I_m indicate a less multifractal nature, and as I_m approaches zero, the system approaches a uniform distribution across the plane (e.g. saturation). Put another way, $\varphi_c = \varphi_i = 2$ indicates a space-filling object with a Euclidean dimension of 2, or a plane.

I_m for the two model runs decreases steadily with increasing extension (Fig. 12D), tending toward uniformity, again consistent with the numerical predictions of Cowie et al. (1995). This is also consistent with the data presented in Fig. 7, where the power-law (fractal) size distribution gives way to exponential, with the system thus becoming less multifractal. It is also consistent with the spacing data, which indicate more regular fault spacings with extension. Finally, for a given extension value, I_m is lower in the thin model, also consistent with data in Fig. 7.

3.9. Mechanical-layer thickness as a boundary condition

Throughout this section we have provided data on a thick and a thin model. Given equal amounts of extension, almost every parameter varies as a function of the model (i.e. mechanical layer) thickness. Based on additional models run for this project (not discussed here in detail), several of these parameters can be related to the thickness of the mechanical layer, t_m. The extension at which the transition

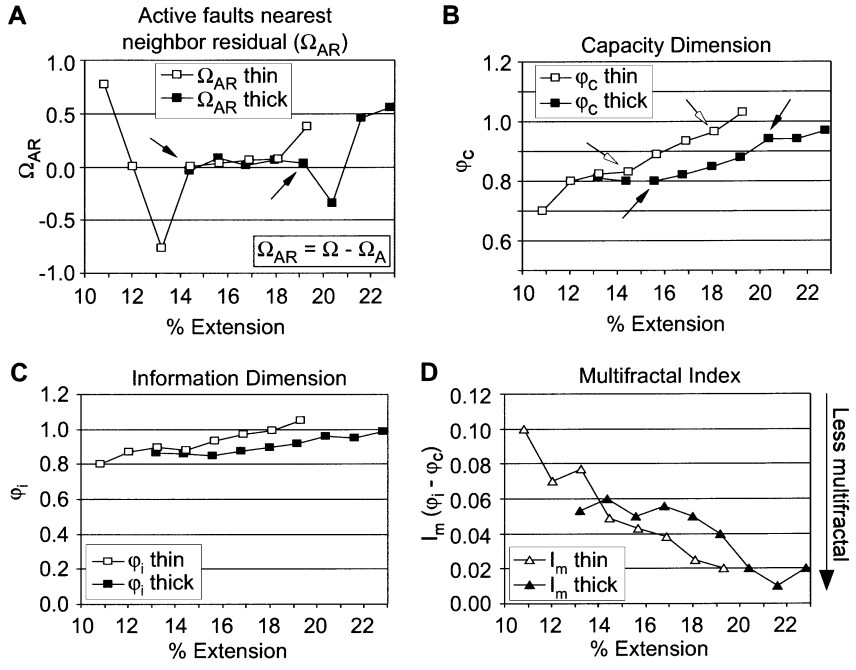

Fig. 12. (A) Residuals for nearest neighbor statistic for active faults. Note that Ω_{AR} approaches zero at the same strain for both the thin and thick models, and that the departure of Ω_{AR} from zero is coeval with an increase in the relative abundance of inactive faults (F_i, Fig. 3B). (B) Fractal (capacity) dimension for both model runs. (C) Fault length-weighted information dimension. (D) Multifractal index ($I_m = \varphi_i - \varphi_c$). Decreasing values of I_m indicate that the system is becoming less multifractal. Recall that a multifractal system is one where a fractal size-frequency distribution overprints a fractal geometric (fault) pattern. Fractal size distributions arise in systems with strong spatial correlations (e.g. Cowie et al., 1995). Systems with an I_m value of 0 actually have a uniform spatial distribution. Arrows point to inflections discussed in text.

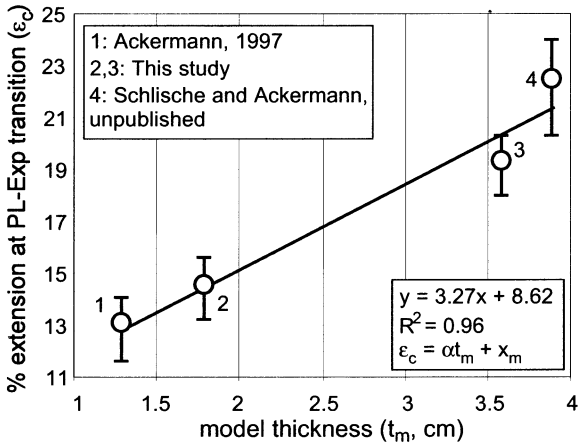

Fig. 13. Strain at the power-law–exponential transition in terms of mechanical layer thickness (t_m). Error bars indicate lowest possible and highest possible strains for transition (based on difficulty with interpreting the cumulative frequency data).

from a power-law to an exponential distribution of fault sizes occurs (ϵ_c) is clearly a function of mechanical layer thickness (Fig. 13). This yields the generalized relation:

$$\epsilon_c = \alpha t_m + x_m \tag{9}$$

where α and x_m are constants. They are probably similar to γ (related to rock properties, Cowie and Scholz (1992a,b)) in the fault length-displacement scaling equation. A relationship can also be defined for the total number of faults observed in the system at any given strain increment:

$$\Delta T = \xi \Delta t_m + y_m \tag{10}$$

where ΔT is the difference in the total number of faults as a function of the difference in mechanical layer thickness (Δt_m) and ξ and y_m are constants. These two relations are best expressed as linear functions, whereas the relationship for the difference in average observed fault length (ΔL_{avg}) is best expressed as a power-law:

$$\Delta L_{avg} = z_m \Delta t_m^{-\kappa} \tag{11}$$

where z_m and κ are constants in the same sense as α, ξ, x_m, and y_m.

3.10. Data summary

We have presented our experimental results in terms of four broad categories: fault activity, fault lengths, the spatial distribution of structures, and the fractal characteristics of the system. The general trends seen in the data are summarized in Fig. 14A in terms of these four categories. With increasing extension, fault length, growth, and linkage all increase, whereas fault nucleation decreases. The proportion of active faults starts off high, but then converges with that of inactive faults (also suggested by Wojtal (1996)). Faults lengthen more per unit displacement, become closer together and more regularly spaced, and large faults contribute relatively more to discontinuous strain accommodation. Finally, the system becomes less multifractal and more homogeneous.

We can also relate the data to mechanical-layer thickness (Fig. 14B). With increasing layer thickness (t_m), the following parameters decrease: sum of the fault lengths, average fault length, characteristic fault length, total number of faults, multifractal index, and average fault spacing (ΣL, L_{avg}, $\langle L \rangle$, L_{max}, F_T, I_m, and s_{avg}, respectively. As t_m increases, the following parameters also increase: fragmentation dimension, length-displacement scaling exponent, capacity dimension, and information dimension (φ_f, n, φ_c and φ_i, respectively). Finally, in thicker layers, the onset of fault linkage, the power-law to exponential transition, and changes in statistical trends all occur at higher extension.

4. Discussion

4.1. Why this evolution of the system?

One of the most striking aspects of our data is the transition of the fault size-frequency distribution from power-law to exponential, also produced experimentally by Spyropoulos et al. (1999) and observed in the field by Gupta and Scholz (2000). Populations of unconstrained faults (contained entirely within a layer) are typically reported as following power-law size distributions. Constrained faults (spanning the layer) appear to follow an exponential size distribution. Cowie et al. (1994) suggested that the different distributions are a function of the width of the fault generation zone (short dimension of the faulted region in map view) relative to the longest faults, which in turn governs the degree to which faults can interact elastically, or 'feel' each other at range. A. Sornette et al. (1990) and D. Sornette et al. (1990) first suggested that the algebraic decay of stress perturbations in the elastic strain field of a volume produce interactions, and thus correlations, at long range. They suggested that this is a result of the threshold nature of brittle faulting and the distribution of strain perturbations (following elasticity equations). This is their explanation for the fractal size and spatial distributions so often observed; fractal (power-law) distributions arise in systems with strong spatial correlations (Cowie et al., 1994).

Rather than the width of the fault generation zone impacting fault interaction and size-frequency distributions, we suggest that the changes in the map pattern and different types of size distributions found in our models hinge on mechanical layer thickness (recall that the width of the fault generation zone was held constant in the experiments). We suggest that this is a boundary condition that accelerates the processes of stress shadowing and crack development described in Spyropoulos et al. (1999). In the model of Ackermann and Schlische (1997), the largest (constrained) faults (those that have ruptured through the entire mechanical layer) continue to grow in length but not in

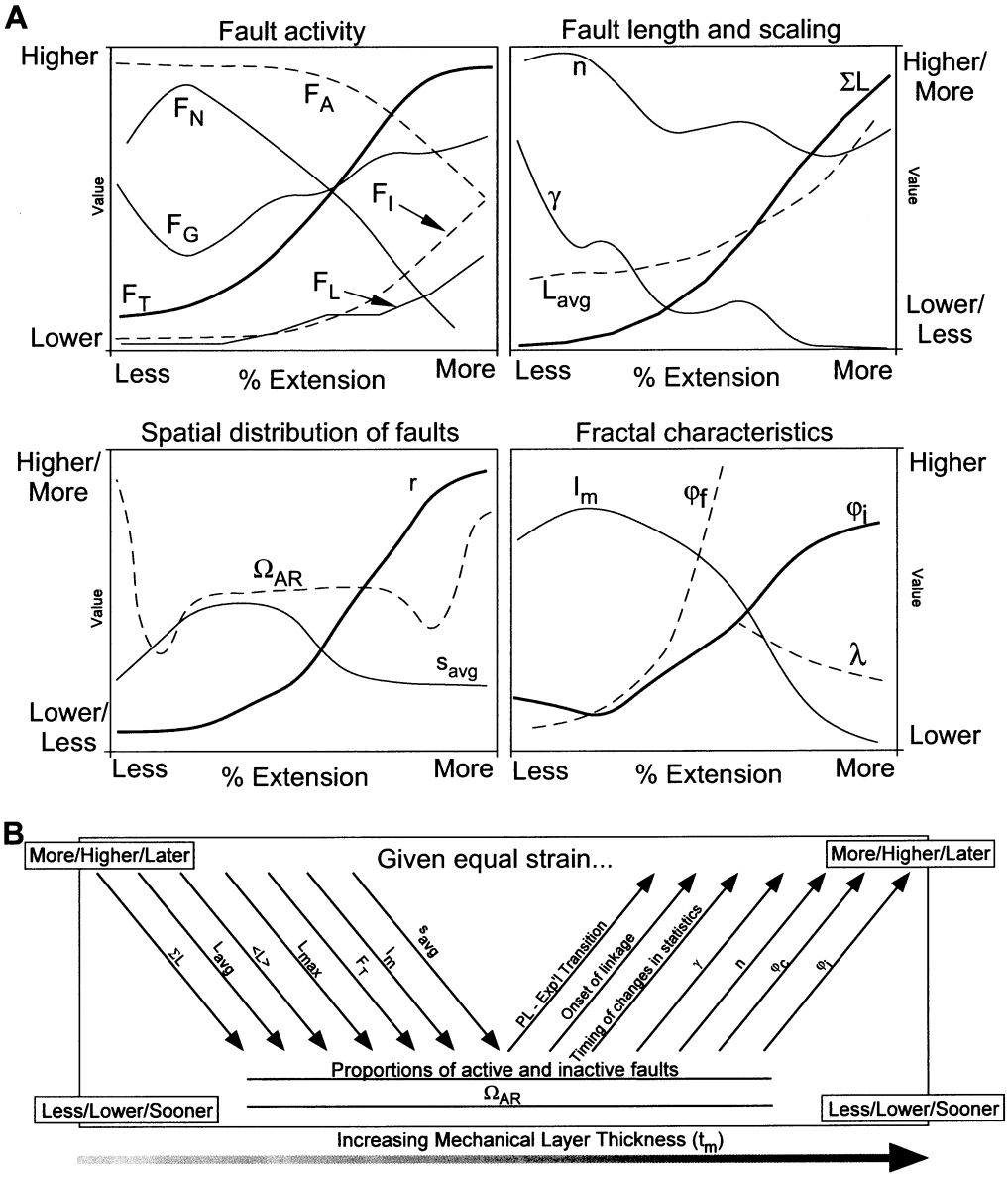

Fig. 14. Summary of data observations for the thin and thick model runs. (A) Generalized trends of statistical and spatial parameters during the structural evolution of the system. (B) Variations in the same parameters as a function of mechanical layer thickness, given an equal amount of strain.

displacement. Displacement profiles change from bell-shaped to flat-topped (see Dawers, 1996; Dawers et al., 1993). The dimensions of the elastic deformation fields (Gupta and Scholz, 1998) and stress-reduction shadows (Willemse, 1997; Spyropoulos et al., 1999) around those faults will be restricted because they scale linearly with displacement (Fig. 15) (Ackermann and Schlische, 1997), and long-range fault interaction will be retarded. Increased rates of along-strike propagation may lead to an increase in lateral fault linkage, such that the end result is a series of large faults with a quasi-regular spacing. Jackson and White (1989) observed a characteristic spacing for faults in the Basin and Range, where the lithosphere is thin.

Nicol et al. (1996) noted that non-power law scaling may indicate that different processes or controls are effective at different scales. We suggest that the exponential distribution develops as fault interaction is suppressed. The strain at which the power-law–exponential transition occurs would be a function of the thickness of the mechanical layer (t_m), since the dimension of the stress reduction shadow scales linearly with displacement (Fig. 15A) (Ackermann and Schlische, 1997), and bigger faults are required to span thicker layers. Exponential size distributions have been found in several areas where faults are believed to span the mechanical layer: Basin and Range (brittle crust, Yu and Scholz, unpublished data); Volcanic Tablelands (Bishop Tuff, N. Dawers, pers. commun.); main trace of San Andreas fault (brittle crust, Wallace, 1973); and Ellis Idaho (small faults in unnamed formation, Ackermann and Schlische, 1999). Note that Wojtal (1996) suggested that

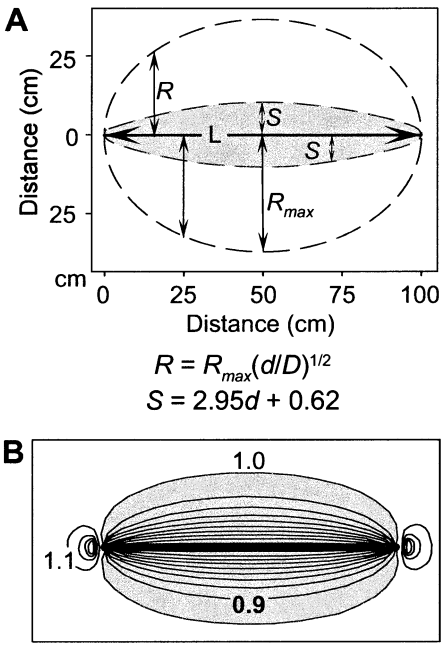

Fig. 15. Comparison of fault shields, deformation fields, and stress-reduction shadows around a normal fault. (A) Relationship between fault shield width (S) and deformation field width (i.e. reverse drag width, R; Gibson et al., 1989) for an idealized fault of length 100 cm and displacement 3 cm. S is based on the empirical relationship in Ackermann and Schlische (1997). R_{max} is equal to the mean of the radii of the fault surface ellipse (in this case, the radii are 50 and 25 cm, and thus the aspect ratio is 2:1). (B) Perturbation of the stress field surrounding a vertical fault (aspect ratio 2:1) following a uniform stress drop. The shear stress component acting parallel to the slip vector is reduced in the shaded areas and enhanced in the unshaded areas. Modified from Willemse (1997). Figure from Ackermann et al. (2001).

fault populations transition from self-similar systems at low extension values to saturated systems at higher extension values.

We have integrated our observations, some of the numerical predictions of Cowie et al. (1995), and the Ackermann and Schlische (1997) model into a three-stage conceptual framework, shown in Fig. 16. The Cowie et al. (1995) model does not include distributed deformation, whereas ours does. Their model begins at $\ll 1\%$ discontinuous deformation and proceeds to $\sim 4\%$. In our models, the first localized faults are visible on the model surface at $\sim 10\%$ extension, but there is not really a map pattern until ~ 13–14%. If we assume that the first 10% extension for our models represents essentially distributed deformation, we can 'remove' it and compare our work with that of Cowie et al. (1995). We see that our early stages overlap with their late stages. Recall that we see many of the same trends they found in our models as well. Elements from Cowie et al. (1995) included in Fig. 16 are a size-frequency distribution that changes from exponential to power-law and a system that becomes more multifractal with increasing strain.

At low extension in Stage I, very few faults exist. They do not interact because their stress reduction shadows are very small relative to the distance between faults. Thus, the size distribution is exponential (Cowie et al., 1995), and faults are randomly distributed according to preexisting flaws. Many faults are born during this early stage to accommodate the strain. The faults exhibit a linear relationship between length and displacement since they are unconstrained and free to grow in all directions. As the faults grow larger and more numerous, they begin to feel each other elastically through their strain fields and stress reduction shadows (*sensu* Davy et al., 1992), and the system moves into Stage II.

As the faults interact (repulsively), power-law (fractal) scaling and self-organization arise, eventually to a multifractal (Cowie et al., 1995; this study). The map distribution becomes non-random, but inherits a random overprint caused by the original distribution of structures (Fig. 16). As the faults grow larger, many of them span the mechanical layer (t_m) and become constrained structures (Ackermann and Schlische, 1997) (Fig. 16), having lost the freedom to grow vertically. These faults can no longer displace as they did before, so the size of their elastic deformation fields is restricted. This in turn retards their ability to interact with other faults, and the system begins to lose its multifractal nature as the exponential size-frequency distribution returns. The size distribution may actually be a mixture of power-law and exponential, such as gamma, as found by Davy (1993) for the San Andreas fault system. Strain must still be accommodated, so faults lengthen more quickly (similar in concept to preferential growth in Bohnenstiehl and Kleinrock (1999)) and link with each other (there may also be intrablock rotation, *sensu* Gross et al., 1997b). This accelerated growth in the strike direction without significant growth in the dip direction leads to a breakdown in length-displacement scaling, with $n < 1$. Finally, the restricted dimensions of relaxed regions (Willemse, 1997) around faults leads to spatial in-filling and more closely spaced faults.

During Stage III, faults are regularly spaced as a function of mechanical layer thickness. The system achieves a saturated state, where fault spacing stops evolving and remains roughly constant (*sensu* Wu and Pollard, 1995) (Fig. 16). Most faults are constrained and follow a length-displacement scaling relationship where $n < 1$. The size distribution is exponential, and there is no multifractal nature, reflecting the suppression of fault interaction. Major faults accommodate most of the strain, such that the proportion of active structures decreases and they no longer appear to dominate the spatial distribution of faults.

4.2. Manifestation of the model

Mechanical layer thickness appears to be a fundamental control on the nature and extent of fault interaction, but not the only one. We suggest that the strain at which a system changes from Stage I to Stage II to Stage III varies, depending in part on the mechanical layer thickness. For example, consider two identical mechanical layers of different thickness that have undergone the same amount of extension. The

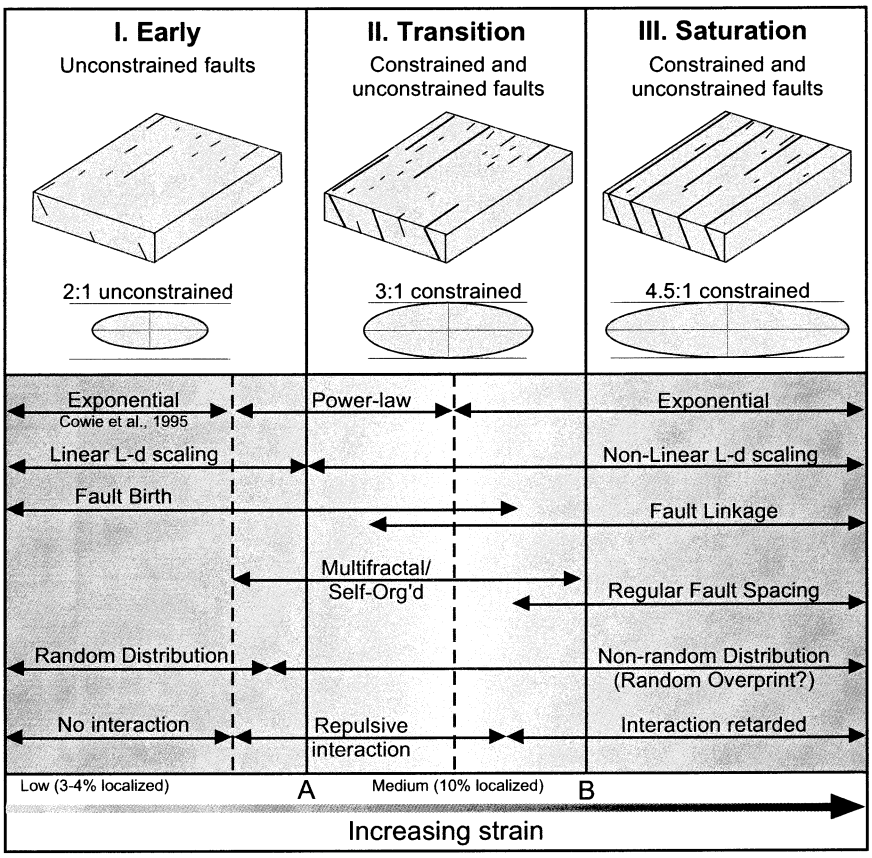

Fig. 16. Conceptual framework for the evolution of simple normal fault systems. Schematic diagrams of fault geometries and structural configurations for the three stages discussed in the text are keyed to the statistical evolution of the system; strain increases from left to right. Constrained faults are restricted to a discrete mechanical layer. Fault-plane views show how fault aspect ratios change when faults become constrained.

thin layer might be in Stage II, whereas the thick layer may still be in Stage I. Interbedded rocks with different material properties (mechanical stratigraphy, *sensu* Gross, 1995) will produce an even more pronounced effect.

Most faults in nature are not restricted to a single mechanical layer. As faults grow and encounter mechanical contrasts, many eventually propagate through the mechanical layer. The system may therefore evolve as I–II–III–II–III, a potential explanation for the dual power-law distribution of Ackermann and Schlische (1997) — two sets of faults, both in Stage II, but seeing different mechanical layer boundaries. This may explain why much of the published cumulative frequency data are noisy and difficult to interpret.

Mechanical stratigraphy can occur from the bed to crustal scale (e.g. Gross, 1995; Ackermann et al., 2001). Thus, these changes and model stages may occur at multiple scales. For example, there may be long-inactive, small-scale (intrablock) systems that exhibit Stage III characteristics. At the same time, larger structures exhibit Stage II characteristics. It may be that the data sampling artifacts and restrictions that challenge so many geoscientists actually prevent us from sampling the true complexity of systems, making it simpler for us to interpret the data at the scale of interest (e.g. prospect or reservoir). Finally, to return to a question posed in the Introduction: are there bounds to scale invariant behavior? We suggest that there are, and that the bounds are a function of effective mechanical layer thickness and rock properties, as suggested by Mandlebrot (1983).

5. Summary

Using experimental models to study the geometric and mathematical evolution of normal fault systems, we have made the following key observations.

1. *With increasing extension*: (a) cumulative fault length, average fault length, the number of faults in the system, and fault-linkage activity all increase; (b) the proportion of active structures decreases and converges with that of inactive structures; (c) faults lengthen more per unit displacement such that their length-displacement scaling is not only non-linear, but dynamic; (d) faults become more closely and regularly spaced, and large faults contribute increasingly to discontinuous strain accommodation; (e) the size-frequency distribution of fault lengths transitions from power-law (fractal) to exponential; (f) the system becomes less multifractal and more homogeneous.

2. *With increasing mechanical layer thickness*: (a) faults are shorter, less elliptical, and farther apart; (b) length-displacement scaling is closer to linear; (c) small faults contribute relatively more to discontinuous strain accommodation; (d) the onset of fault linkage, the power-law to exponential transition, and other changes in statistical trends occur at higher strains.
3. Many of these observations validate the predictions of numerical (e.g. Cowie et al., 1993, 1995) and geometric models (e.g. Cladouhos and Marrett, 1996) for normal fault growth and system evolution, and are consistent with the results of the recent experimental work of Spyropoulos et al. (1999) and field work of Gupta and Scholz (2000).
4. We suggest that these trends reflect the control that mechanical layer thickness may exert on fault interaction and, thus, scaling by effectively suppressing fault interaction when faults span and are restricted to a mechanical layer. This can be described using a three-stage model that integrates aspects of Cowie et al. (1995) and Ackermann and Schlische (1997). In this model, size-frequency distributions change from exponential to power law to exponential, and the system itself changes from fractal to multifractal to fractal, and ultimately homogeneous (saturated). This results from a transition from limited fault interaction to interaction to retarded interaction as the system approaches saturation.
5. We believe that a natural system will not simply progress from Stage I to II to III. Rather, a system will oscillate between Stages II and III as faults encounter and then exceed mechanical layer boundaries.
6. The existence of mechanical stratigraphy (*sensu* Gross, 1995) will lead to different system scaling attributes at different structural levels as a function of layer thickness and rheology.
7. Our data support the existence of upper and lower bounds for the scale invariant behavior of fault systems, and that these bounds likely scale with mechanical layer thickness and rheology, as reported by Mandelbrot (1983) for natural fractures.

Acknowledgements

We thank Mobil Technology Company for its support during this study. Ackermann thanks ExxonMobil Upstream Research Company for permission to publish this work. Karen Bemis, Amy Clifton, Patience Cowie, Nancye Dawers, Gloria Eisenstadt, Mike Gross, Anu Gupta, Peter Hennings, Paul Olsen, Peter Rona, Michelle Seidl, Chrysanthe Spyropoulos, and Mike Viersma provided valuable insight, advice, or discussion regarding the modeling process and subsequent data interpretation. Jim Carpenter, Chuck Kiven, and Laird Thompson reviewed an early version of this manuscript. This work benefited from a thoughtful review by Steve Wojtal and the insights of an anonymous reviewer. Schlische was supported by NSF grant EAR-9706199.

References

Ackermann, R.V., 1997. Spatial distribution of rift-related fractures: field observations, experimental modeling, and influence on drainage networks. Ph.D. dissertation, Rutgers University, New Brunswick, NJ.

Ackermann, R.V., Schlische, R.W., 1997. Anticlustering of small normal faults around larger faults. Geology 25, 1127–1130.

Ackermann, R.V., Schlische, R.W., 1999. Uh-oh! $n < 1$: Dynamic length-displacement scaling. Eos, Transactions, American Geophysical Union 80, S328.

Ackermann, R.V., Schlische, R.W., Patiño, L.C., Johnson, L.A., 2001. A Lagerstätte of rift-related tectonic structures from the Solite Quarry, Dan River/Danville rift basin. In: LeTourneau, P.M., Olsen, P.E. (Eds.). Aspects of Triassic–Jurassic Rift Basin Geoscience. Columbia University Press, New York, in press.

Bohnenstiehl, D.R., Kleinrock, M.C., 1999. Faulting on the median valley floor of the trans-Atlantic geotraverse (TAG) segment, 26°N on the Mid-Atlantic Ridge. Journal of Geophysical Research 104, 29,351–29,364.

Cartwright, J.A., Trudgill, B.D., Mansfield, C.S., 1995. Fault growth by segment linkage: an explanation for scatter in maximum displacement and trace length data from the Canyonlands. Journal of Structural Geology 17, 1319–1326.

Cladouhos, T.T., Marrett, R., 1996. Are fault growth and linkage models consistent with power-law distributions of fault lengths? Journal of Structural Geology 18, 281–293.

Clifton, A.E., Schlische, R.W., Withjack, M.O., Ackermann, R.V., 2000. Influence of rift obliquity on fault-population systematics: results of clay modeling experiments. Journal of Structural Geology 22, 1491–1509.

Cloos, H., 1928. Experimente zur inneren tektonik. Centralblatt fur Mineralogie, Abt. B, 609–621.

Cloos, H., 1930. Kunstliche gebirge, II. Natur und Museum 60, 258–269.

Cloos, E., 1968. Experimental analysis of Gulf Coast fracture patterns. AAPG Bulletin 52, 420–444.

Cowie, P.A., 1998. A healing-reloading feedback control on the growth rate of seismogenic faults. Journal of Structural Geology 20, 1075–1088.

Cowie, P.A., Scholz, C.H., 1992a. Physical explanation for displacement-length relationship of faults using a post-yield fracture mechanics model. Journal of Structural Geology 14, 1133–1148.

Cowie, P.A., Scholz, C.H., 1992b. Displacement-length scaling relationship for faults: data synthesis and discussion. Journal of Structural Geology 14, 1149–1156.

Cowie, P.A., Shipton, Z.K., 1998. Fault tip displacement gradients and process zone dimensions. Journal of Structural Geology 20, 983–997.

Cowie, P.A., Vanneste, C., Sornette, D., 1993. Statistical physics model for the spatiotemporal evolution of faults. Journal of Geophysical Research 98, 21,809–21,821.

Cowie, P.A., Malinverno, A., Ryan, W.B.F., Edwards, M.H., 1994. Quantitative fault studies on the East Pacific Rise: a comparison of sonar imaging techniques. Journal of Geophysical Research 99, 15,205–15,218.

Cowie, P.A., Sornette, D., Vanneste, C., 1995. Multifractal scaling properties of a growing fault population. Geophysical Journal International 122, 457–469.

Cressie, N.A.C., 1993. Statistics for Spatial Data. John Wiley and Sons, New York, 900pp.

Davy, P., 1993. On the fault-length frequency distribution of the San Andreas fault system. Journal of Geophysical Research 98, 12,141–12,151.

Davy, P., Sornette, A., Sornette, D., 1992. Experimental discovery of

scaling laws relating fractal dimensions and the length distribution exponent of fault systems. Geophysical Research Letters 19, 361–363.

Davy, P., Hansen, A., Bonnet, E., Zhang, S.-Z., 1995. Localization and fault growth in layered brittle-ductile systems: implications for deformations of the continental lithosphere. Journal of Geophysical Research 100, 6281–6294.

Dawers, N.H., 1996, Observations of fault-growth scaling relations. Ph.D. thesis, Columbia University, New York.

Dawers, N.H., Anders, M.H., 1995. Displacement-length scaling and fault linkage. Journal of Structural Geology 17, 607–614.

Dawers, N.H., Anders, M.H., Scholz, C.H., 1993. Fault length and displacement: scaling laws. Geology 21, 1107–1110.

Eisenstadt, G., Withjack, M.O., 1995. Estimating inversion: results from clay models. Geological Society of London Special Publication 88, pp. 119–136.

Ellis, P.G., McClay, K.R., 1988. Listric extensional fault systems—results of analogue model experiments. Basin Research 1, 55–70.

Fossen, H., Gabrielsen, R.H., 1996. Experimental modeling of extensional fault systems by use of plaster. Journal of Structural Geology 18, 673–688.

Fossen, H., Hesthammer, J., 1997. Geometric analysis and scaling relations of deformation bands in porous sandstone. Journal of Structural Geology 17, 1479–1493.

Gauthier, B.D.M., Lake, S.D., 1993. Probabilistic modeling of faults below the limit of seismic resolution in Pelican Field, North Sea, Offshore United Kingdom. AAPG Bulletin 77, 761–777.

Gibson, J.R., Walsh, J.J., Watterson, J., 1989. Modelling of bed contours and cross-sections adjacent to planar normal faults. Journal of Structural Geology 11, 317–328.

Gillespie, P.A., Walsh, J.J., Watterson, J., 1992. Limitations of dimension and displacement data from single faults and the consequences for data analysis and interpretation. Journal of Structural Geology 14, 1157–1172.

Gross, M.R., 1995. Fracture partitioning: failure mode as a function of lithology in the Monterey Formation of Coastal California. Geological Society of America Bulletin 107, 779–792.

Gross, M.R., Becker, A., Gutiérrez-Alonso, G., 1997a. Transfer of displacement from multiple slip zones to major detachment in an extensional regime: example from the Dead Sea Rift, Israel. Geological Society of America Bulletin 109, 1021–1035.

Gross, M.R., Gutiérrez-Alonso, G., Bai, T., Wacker, M.A., Collinsworth, K.B., 1997b. Influence of mechanical stratigraphy and kinematics on fault scaling relations. Journal of Structural Geology 19, 171–183.

Gupta, A., Scholz, C.H., 1998. Utility of elastic models in predicting fault displacement fields. Journal of Geophysical Research 103, 823–834.

Gupta, A., Scholz, C.H., 2000. Brittle strain regime transition in the Afar depression: implications for fault growth and seafloor spreading. Geology 28, 1087–1090.

Hubbert, M.K., 1937. Theory of scale models as applied to the study of geologic structures. Geological Society of America Bulletin 48, 1459–1519.

Jackson, J.A., White, N.J., 1989. Normal faulting in the upper continental crust: observations from regions of active extension. Journal of Structural Geology 11, 15–36.

Kakimi, T., 1980. Magnitude-frequency relation for displacement of minor faults and its significance in crustal deformation. Bulletin of the Geological Society of Japan 31, 467–487.

Kautz, S.A., 1987. The importance of cryptic extension in scale models of normal faulting: unpublished M.Sc. thesis, University of Texas at Austin, 75pp.

Kautz, S.A., Sclater, J.G., 1988. Internal deformation in clay models of extension by block faulting. Tectonics 7, 823–832.

Mandlebrot, B.B., 1967. How long is the coast of Britain? Statistical self-similarity and fractional dimension. Science 156, 636–638.

Mandlebrot, B.B., 1983. The Fractal Geometry of Nature. Freeman, San Francisco, 468pp.

Marchal, D., Guiraud, M., Rives, T., Van den Driessche, J., 1998. Space and time propagation processes of normal faults. In: Jones, G., Fisher, Q.J., Knipe, R.J. (Eds.). Faulting, Fault Sealing, and Fluid Flow in Hydrocarbon Reservoirs. Geological Society, London, Special Publication 147, pp. 51–70.

Marrett, R., Allmendinger, R.W., 1991. Estimates of strain due to brittle faulting: sampling of fault populations. Journal of Structural Geology 13, 735–738.

Marrett, R., Allmendinger, R.W., 1992. Amount of extension on "small" faults: an example from the Viking graben. Geology 20, 47–50.

Marrett, R., Ortega, O.J., Kelsey, C.M., 1999. Extent of power-law scaling for natural fractures in rock. Geology 27, 799–802.

Nalpas, T., Brun, J.-P., 1993. Salt flow and diapirism related to extension at crustal scale. Tectonophysics 228, 349–362.

Nicol, A., Walsh, J.J., Watterson, J., Gillespie, P.A., 1996. Fault size distributions — are they really power-law? Journal of Structural Geology 18, 191–199.

Oertel, G., 1965. The mechanism of faulting in clay experiments. Tectonophysics 2, 343–393.

Pickering, G., Bull, J.M., Sanderson, D.J., 1995. Sampling power-law distributions. Tectonophysics 248, 1–20.

Pickering, G., Peacock, D.C.P., Sanderson, D.J., Bull, J.M., 1997. Modeling tip zones to predict the throw and length characteristics of faults. AAPG Bulletin 81, 82–99.

Rives, T., Razack, M., Petit, J.-P., Rawnsley, K.D., 1992. Joint spacing: analogue and numerical simulations. Journal of Structural Geology 14, 925–937.

Schlische, R.W., Young, S.S., Ackermann, R.V., Gupta, A., 1996. Geometry and scaling relations of a population of very small rift-related normal faults. Geology 24, 683–686.

Scholz, C.H., Contreras, J.C., 1998. Mechanics of continental rift architecture. Geology 26, 967–970.

Scholz, C.H., Cowie, P.A., 1990. Determination of total strain from faulting using slip measurements. Nature 346, 837–838.

Scholz, C.H., Dawers, N.H., Yu, J.-J., Anders, M.A., Cowie, P.A., 1993. Fault growth and fault scaling laws: preliminary results. Journal of Geophysical Research 85, 21,951–21,961.

Sims, D., 1993. The rheology of clay: a modeling material for geologic structures. Eos, Transactions, American Geophysical Union 74 (46), 569 (supplement).

Sornette, D., Davy, P., 1991. Fault growth model and universal fault length distribution. Geophysical Research Letters 18, 17353–17361.

Sornette, A., Davy, P., Sornette, D., 1990. Growth of fractal fault patterns. Physics Review Letters 65, 2266–2269.

Sornette, A., Davy, P., Sornette, D., 1993. Fault growth in brittle-ductile experiments and the mechanics of continental collisions. Journal of Geophysical Research 98, 12,111–12,139.

Sornette, D., Davy, P., Sornette, A., 1990. Structuration of the lithosphere in plate tectonics as a self-organized critical phenomenon. Journal of Geophysical Research 95, 17,353–17,361.

Spyropoulos, C., Griffith, W.J., Scholz, C.H., Shaw, B.E., 1999. Experimental evidence for different strain regimes of crack populations in a clay model. Geophysical Research Letters 26, 1081–1084.

Stauffer, D., Aharony, A., 1992. Introduction to Percolation Theory. 2nd Ed. Taylor and Francis, London, 181pp.

Swan, A.R.H., Sandilands, M., 1995. Introduction to Geological Data Analysis. Blackwell Science, Oxford, 446pp.

Trudgill, B., Cartwright, J., 1994. Relay-ramp forms and normal fault linkages, Canyonlands National Park, Utah. Geological Society of America Bulletin 106, 1143–1157.

Vendeville, B., 1987. Champs de failles et tectonique en extension: modélisation expérimentale. Ph.D. thesis, Université de Rennes (France), 395pp.

Vendeville, B.C., Ge, H., Jackson, M.P.A., 1995. Scale models of salt tectonics during basement-involved extension. Petroleum Geoscience 1, 179–183.

Viersma, M.G., 1997. Variations in strain accommodated by faults in a

scaled physical model. Independent Study Project Report, Rutgers University, New Brunswick, NJ.

Villemin, T., Angelier, J., Sunwoo, C., 1995. Fractal distribution of fault length and offsets: implications of brittle deformation evaluation—Lorraine Coal Basin. In: Barton, C.C., La Pointe, P.R. (Eds.). Fractals in the Earth Sciences. Plenum Press, New York, pp. 205–226.

Wallace, R.E., 1973, Surface fracture patterns along the San Andreas Fault. Proceedings from the Conference on Tectonic Problems of the San Andreas Fault System. Stanford University Publications, Geological Sciences, 13, pp. 248–250, illus.

Walsh, J.J., Watterson, J., 1988. Analysis of the relationship between displacements and dimensions of faults. Journal of Structural Geology 10, 239–247.

Walsh, J., Watterson, J., Yielding, G., 1991. The importance of small-scale faulting in regional extension. Nature 351, 391–393.

Watterson, J., 1986. Fault dimensions, displacements and growth. Pure and Applied Geophysics 124, 365–373.

Weijemars, R., Jackson, M.P.A., Vendeville, B., 1993. Rheological and tectonic modeling of salt provinces. Tectonophysics 217, 143–174.

Willemse, E.J.M., 1997. Segmented normal faults: correspondence between three-dimensional mechanical models and field data. Journal of Geophysical Research 102, 675–692.

Withjack, M.O., Callaway, J.S., 2000. Active normal faulting beneath a salt layer: An experimental study of deformation in the covers sequence. AAPG Bulletin, 84, 627–652.

Withjack, M.O., Jamison, W.R., 1986. Deformation produced by oblique rifting. Tectonophysics 126, 99–124.

Withjack, M., Islam, Q., LaPointe, P., 1995. Normal faults and their hanging wall deformation—an experimental study. AAPG Bulletin 79, 1–18.

Wojtal, S.F., 1994. Fault scaling laws and the temporal evolution of fault systems. Journal of Structural Geology 16, 603–612.

Wojtal, S.F., 1996. Changes in fault displacement populations correlated to linkage between faults. Journal of Structural Geology 18, 265–280.

Wu, H., Pollard, D.D., 1995. An experimental study of the relationship between joint spacing and layer thickness. Journal of Structural Geology 17, 887–905.